Fast firing of 3 mol% yttria-stabilized zirconia: On the effect of heating rate on sintering

Mattia Biesuz, Emanuele de Bona, Charles Manière

Fast firing of 3 mol% yttria-stabilized zirconia: *On the effect of heating rate on sintering*

Mattia Biesuz[1,2,#], Emanuele De Bona[1], Charles Manière[3]

[1] Department of Industrial Engineering, University of Trento, Via Sommarive 9, 38123, Trento, Italy

[2] INSTM, Via G. Giusti 9, Firenze 50121, Italy

[3] ENSICAEN, UNICAEN, CNRS, CRISMAT, Normandie Univ, Caen, France

[#] Corresponding author, M.B. mattia.biesuz@unitn.it; (+39) 0461 283551

C.M. charles.maniere@ensicaen.fr; +33 (0)2 31 45 13 69

Abstract

The impact of rapid heating on sintering is currently getting a growing scientific interest. Previous results have shown that when considering 90 nm-sized 3 mol% yttria-stabilized zirconia (3YSZ) powder the heating rate effect on densification is not detectable, whereas it is huge when using finer powder (≈20 nm, specific surface area, SSA = 30-60 $m^2 g^{-1}$). Herein, we investigate the fast firing of ≈40 nm 3YSZ powder (SSA = 16 $m^2 g^{-1}$) and compare it with conventional sintering. The results show that the heating rate has a modest effect on the final density with improvements always below 2-3% in terms of relative density. The relatively good match between fast firing and the densification behavior predicted by the master sintering curves agrees with the observed microstructural evolution, where fast-firing provides only a modest effect on the pore size. Finally, it is shown that the heating rate does not impact the dynamics of closed pore formation.

Keywords: Sintering; fast firing; heating rate; microstructure; master sintering curve

1. Introduction

Rapid sintering of ceramics is attracting a growing technological and scientific interest. Moving ahead from the first pioneering works on fast firing (FF) and direct sintering [1], nowadays several rapid sintering approaches have been developed [2]. These are typically based on the use of electric fields/currents (flash sintering [3–6], spark plasma sintering [7–9], and others [10]) or electromagnetic radiations at the GHz frequencies (microwave sintering [11, 12]). Recently, a renewed interest is currently emerging also thanks to the discovery of the ultrafast high-temperature sintering (UHS) technique in 2020 [13, 14].

Besides the technological interest related to the reduction of the carbon footprint of the ceramic industry, several scientific challenges connected with rapid firing are being investigated. In particular, the mechanistic understanding of “if and how” rapid sintering might enhance densification is an argument of discussion and study. In fact, different phenomena have been proposed to be activated by rapid heating [15–17]:

i. *Enhanced densification over coarsening*: due to the different activation energies for coarsening and densification, rapid heating is expected to favor the process with the highest activation energy. As densification relies on volume or grain boundary diffusion whereas coarsening might take place also via evaporation/condensation and surface diffusion, densification is expected to possess higher activation energy and, therefore, be facilitated by fast heating. This phenomenon is quite

established in the literature [1]. Our recent work on 3 mol% yttria-stabilized zirconia (3YSZ) nanopowder (actual particle size, APS ≈20 nm, SSA = 30-60 $m^2 g^{-1}$) has shown that it holds on for UHS in Ar atmosphere[18]. There we observed a substantial grain refinement at a fixed density level for UHSed 3YSZ compared with artifacts processed by conventional sintering. Some improvements in the sintering behavior under rapid heating were also reported for 8YSZ in UHS, these being associated with an apparent reduction in the activation energy for sintering [19].

ii. *Different pore structures:* Ji et al. [16] observed that YSZ processed by rapid sintering (flash, SHS…) possess pores smaller than the grain size, whereas conventional sintering leads to larger pores coordinated by more grains. The different pore coordination was recently confirmed in 3YSZ nanopowders (APS ≈ 20 nm, SSA = 30-60 $m^2 g^{-1}$) processed by UHS [18].

iii. *Non-relaxed grain boundaries:* Todd et al. have argued that the rapid grain boundary formation might cause the development of out-of-equilibrium interfaces possessing diffusivities different from the conventional ones [17]. Experimental evidence is still very partial [17, 20], though out-of-equilibrium grain boundary morphology have been reported in rapidly sintered alumina [20]

iv. *Melting of surface impurities:* The presence of impurities on the particle surface (carbonates, sulfates, hydroxides…) might also play a role.

These typically decompose before melting in conventional heating conditions, it is not clear whether rapid heating could cause the formation of a transient liquid phase retarding their decomposition [17].

v. *Change in the pore geometry:* The first bullet point mentioned the competition between densification which is activated by grain boundary/lattice diffusion and coarsening which is based on grain growth and surface diffusion. In addition to the temperature regime of these respective mechanisms, surface diffusion has another consequence on the pore morphology that could explain faster densification. Surface diffusion reorganizes the pore shape from initial sharp angles to spheroidized structures less responsive to sintering. This decreases both the sintering stress and the stress intensification factor. Fast firing is expected to decrease this morphology mechanisms that decrease the sintering responsiveness [21, 22].

It is not easy to compare rapid sintering techniques, like fast firing, with conventional sintering is not always easy as the time scale largely differs. The master sintering curve (MSC) model offers a possible approach to evidence the effect of rapid heating on sintering [23]. The MSC theory is based on the assumption that a one-to-one correlation exists between a sintering parameter $\Theta_{(T,t)}$ and the density (ρ):

$$\rho_{(T,t)} = f_{\Theta_{(T,t)}} \qquad (1)$$

with

$$\Theta_{(T,t)} = \int_0^t \frac{\exp(-Q/RT)}{T}\, dt \qquad (2)$$

where T is the absolute temperature, R the ideal gas constant and Q the activation energy for densification. Indeed, if rapid heating plays a role on sintering through any of the mechanisms previously listed, then we expect a deviation from the $\rho - \Theta$ relation extrapolated at low heating rate.

When considering the heating rate effect on the sintering of ceramics, YSZ is probably the most studied material. This correlates with its technological relevance, it being an intriguing structural ceramic characterized by transformation toughening mechanisms (3YSZ) and possessing high oxygen ions conductivity making it a candidate for applications like solid oxide fuel cell electrolytes and oxygen sensors (8YSZ). Besides, YSZ is considered a model system for a wide family of fluorite-structured ceramics. We have recently observed that UHS of 3YSZ nanopowder (APS ≈ 20 nm, SSA = 30-60 $m^2\,g^{-1}$) [18, 23] has a huge effect on the densification behavior, the difference is however not experimentally detectable when considering coarser powder (APS ≈ 90 nm, SSA = 7 $m^2\,g^{-1}$) [24]. Herein we question if rapid heating by fast firing has a strong effect on the densification behavior of 3YSZ with intermediate particle size (APS ≈ 40 nm, SSA = 16 $m^2\,g^{-1}$). The manuscript provides a detailed description of the densification pathway connected with the developed microstructures. The morphological and chemical features of the powder used in this (and previous works used in the Discussion section) are reported in Table S1 of Supplementary material.

2. Experimental procedures

2.1 Samples preparation

Cylindrical pellets (diameter = 13 mm, thickness ≈ 2 mm) were shaped by uniaxially pressing 3YSZ granulated powder (TZ-3YB-E, Tosoh Corporation, Tokyo, Japan) under 220 MPa using a steel die. The green pellets were debinded at 600°C for 30 min in a muffle furnace (Nabertherm GmbH) under a static air atmosphere, the heating and cooling rates were 10 °C min^{-1}. The relative density of the pellets, evaluated by the geometrical method with a caliper (sensitivity 0.01 mm) and an analytical balance (sensitivity 0.1 mg), was around 49%. The theoretical density was assumed 6.12 g cm^{-3} as determined by He pycnometer of the debinded powder (Ultrapyc 5000, Anton Paar, USA).

The debinded samples were then subjected to three different sintering procedures using a Nabertherm GmbH muffle furnace operating in static air: (i) conventional sintering using 10°C min^{-1} as heating and cooling rate and 120 min isothermal-dwell at different temperatures; (ii) fast firing with 120 min dwell and (iii) fast firing with 10 min dwell at the sintering temperature. In the case of fast firing, once the furnace reached the selected sintering temperature it was quickly opened, and the sample was immediately introduced into the hot chamber. For each condition, 2 samples were produced. Note that if a transient liquid phase or non-relaxed grain boundary forms during rapid heating (mechanisms iii and iv in the Introduction), then the sample FFed for 10 min should substantially overperform those fast fired for 120 min, these mechanisms impacting only the first minutes of the process.

2.2 Master sintering curve calculation

The master sintering curve was determined by the dilatometric method using a horizontal Linseis L75 dilatometer equipped with an alumina measurement system. The dilatometric behavior was evaluated at different heating (2.5, 10 and 25 °C min^{-1}) in air. The measurement system applied a load of 0.5 N on the sample during the dilatometric analysis. The MSC was determined by minimizing the deviation of the experimental data in the $\Theta_{(T,t)} - \rho$ plane from a fitting Boltzmann function [25, 26].

2.3 Sintered pellets characterization

The density of the sintered samples was determined by Archimedes' method using an analytical balance Gibertini (Italy) and deionized water as the buoyancy medium. The samples were prepared using the ASTM C830-00(2016) as reference. The open pores size and distribution were evaluated by Hg porosimetry (Porosimeter 2000, Carlo Erba, Italy). The microstructure was studied by polishing and thermally etching the sintered samples. Polishing was carried out using SiC papers (up to grit 4000) and 1 µm diamond paste. The thermal etching was carried out at 10°C min^{-1} with 30 min dwell at different temperatures which were selected on each sample to avoid variations in Θ > 5%. The microstructure was then observed at the sample center with an FE-SEM (Zeiss Supra40). To make the sample conductive, these were coated with a sputtereted Pt-Pd thin film.

2.4 Modelling

The fast-firing approach involves a few minutes of sintering time. Consequently, the thermal history has a high importance and every minute of heating time to reach the furnace equilibrium temperature matters. If the heating time to reach the equilibrium temperature is too long, it should be considered in the calculation of the $\Theta_{(T,t)}$ integral. Estimating the heating kinetics of the sample when inserted into the furnace involves determining the temperature at the sample location in contact with the support. Subsequently, the specimen's thermal conductivity and specific heat were taken into account to estimate the heating curve when placed in the furnace. Two calculations were performed using the COMSOL multiphysics® software. The first was a conductive-convective-radiative simulation of the furnace to estimate the temperature at the support location. To reduce the calculation time, this simulation used a 2D axisymmetric approximation with a geometry using close air/insulation material volume, and the heating elements are placed on the side like in the real box furnace. The geometry is reported in **Figure 1**. The furnace temperature-dependent materials properties are reported in a previous work [27], and the same external convective/radiative boundary conditions are used. The $MoSi_2$ heating element thermal properties were taken from reference [28]. The specimen temperature curve was extracted at the sample support location by this first simulation. Because the furnace simulation is relatively long, the specimen temperature homogenization when entered in the furnace is calculated separately by a thermal simulation limited to the specimen. This second simulation is used to assess the transient heating time and temperature profile. In the latter, the calculated furnace temperature curve is

imposed at the surfaces of the pellet to simulate the heating. The pellet relative density during the heating stage is assumed to correspond to the initial relative density. Consequently, the thermal conductivity used an effective medium approximation formula [29] to estimate the conductivity at 50% density ($\kappa_{porous} = \kappa_{dense}(-0.5 + 1.5\rho)$) from the fully dense value (κ_{dense}) with, ρ the relative density. To represent the heating schedule, a virtual probe is located at the pellet center to record the temperature. The equilibrium stage is attained when the temperature at the center is the same as in the surface.

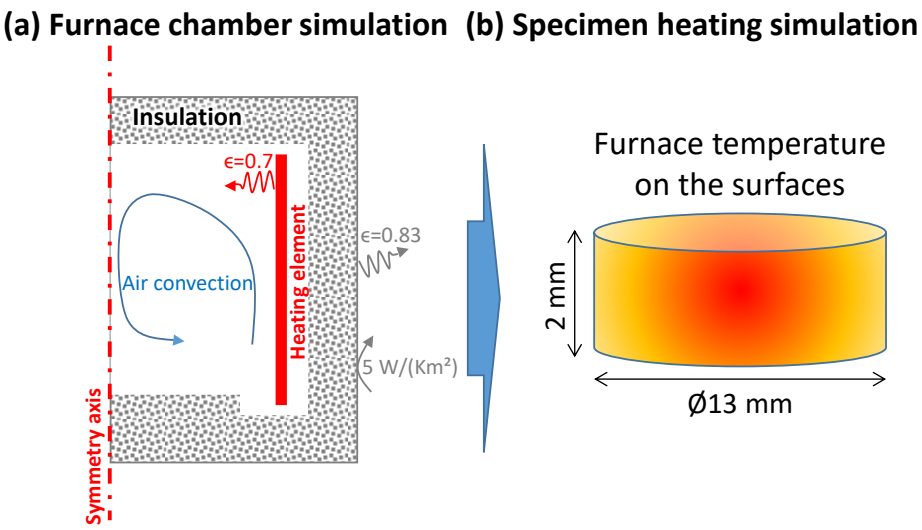

Figure 1. Specimen heating simulation with (a) the furnace chamber (a) and the specimen model.

Plotting the relative densities for fast-fired materials together with the master sintering curve helps to reveal the dissimilarities with the conventional behavior. The underlying sintering model for the dominant sintering mechanism is the following [23].

$$\frac{1}{3\rho}\frac{d\rho}{dt} = \frac{\gamma\Omega\Gamma(\rho)D_0}{kTG^m}exp\left(\frac{-Q}{RT}\right) \quad (3)$$

with, γ the surface energy, Ω the atomic volume, D_0 the constant term of the coefficient of diffusion, the Boltzmann constant, *G* the grain size, and *m* the sintering mechanisms grain size sensitivity. $\Gamma(\rho)$ is a porosity function that relates the mean diffusion distance to other microstructure characteristics like the mean grain size. Except for one exponent, this relative density function is also called the stress intensification factor and is usually independent of the heating schedule unless significant surface diffusion dissimilarity occurs [23]. The first phenomena cited in the introduction (surface diffusion) impact this term. In fast firing, the surface diffusion is expected to be severely reduced leading to more responsive porous geometries with sharp angles, higher stress intensification and driving force.

From the sintering model (**Eq. 3**), it is clear a lower activation energy or a higher stress intensification ($\sim\Gamma(\rho)$) at fixed relative density will result in a higher sintering rate. Final stage grain growth reduction and improvement of the sintering path will also accelerate the sintering. A similar comparison can be made through the master sintering curve, where the previous sintering model is developed in the following equation.

$$\frac{k}{3\gamma\Omega D_0}\int_{\rho_0}^{\rho}\frac{G(\rho)^m}{\rho\Gamma(\rho)}d\rho = \int_0^t \frac{1}{T}exp\left(\frac{-Q}{RT}\right)dt = \Theta_{(T,t)} \quad (4)$$

This equation helps to understand the expected fast-firing shift in the master sintering curve. If the fast-firing relative densities are plotted assuming the diffusion activation energy (Q) same as conventional sintering, the left-hand side (**Eq. 4**) which is relative density dependent helps interpret the possible dissimilarity with conventional sintering. If at same density, the fast firing reduces the surface diffusion, it implies higher stress intensification ($\Gamma_{fast\ firing} > \Gamma_{conventional}$), then lower value of $\Theta_{(T,t)}$ are expected. This implies a shift of the fast-firing densities to the left in the master sintering curve plot. Similarly, if out-of-equilibrium (or melted) grain boundary phenomena disturb the diffusion coefficient constant term (D_0), the expected impact on the master sintering curve (**Eq. 4**) is also a shift to the left as a result of higher diffusion coefficient. If the latter mechanisms imply lower activation energy, the error on the activation energy will be reported on the denominator of the left-hand side for **Eq 4** which also leads to a shift on the left for the master sintering curve. In conclusion, the shift of the fast-firing relative density values on the left compared to conventional indicates a faster sintering behavior but advanced sintering kinetic characterizations are required to precisely say which term is responsible for this faster kinetics.

3. Results

3.1 Identification of the master sintering curve

The relative density evolution extrapolated by dilatometry at different heating rates is reported in **Figure 2a** as a function of the furnace temperature. The density monotonically increases with temperature and a clear sintering delay can be detected when increasing the heating rate. The three density curves correctly collapse into a single master sintering curve when the density is plotted against $\Theta_{(T,t)}$ (**Figure 2b**). The best result, minimizing the error (inset in **Figure 2b**), was obtained assuming an activation energy for densification of 650 kJ mol^{-1}. The data are properly fitted using a Boltzmann-like function (solid black line in **Figure 2b**).

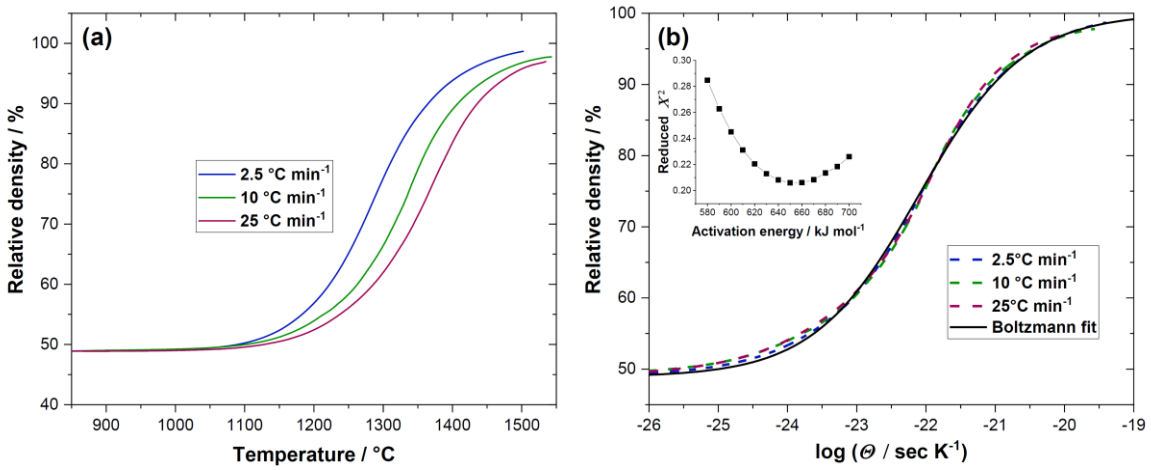

Figure 2. (a) Relative density as a function of the furnace temperature for 3YSZ pellets (40 nm) sintered at different heating rates and (b) master sintering curve (Q = 650 kJ mol^{-1}) extracted from the data in (a). The inset in (b) reports the reduced X^2 as a function of the selected activation energy.

3.2 Density evolution during fast firing and conventional sintering

The bulk and apparent density evolution as a function of the sintering temperature is reported in **Figure 3a** and **Figure 3b**, respectively, whereas **Figure 3c** reports the open porosity. Both bulk density and open porosity show a monotonical trend, coherent with the dilatometric results. The samples fired for 120 min approaches the near full densification starting from 1350°C, whereas indeed sintering is apparently delayed when considering the 10 min treatments due to the shorter processing time. On the other hand, the apparent density is close to the theoretical one at low sintering temperature (all the porosity is open in the early and intermediate sintering stages). In the case of 120 min treatments, it starts dropping at 1250°C, reaches a minimum at 1275°C, and then increases again. Such behavior is consistent with the formation of closed pores in the final sintering stage. Again, the samples treated by the 10 minute-fast firing processes show a similar trend, though shifted at higher temperatures (≈ 100°C).

In general, we can observe that modest differences can be spotted when comparing samples conventionally sintered and FFed for 120 min. However, the fast-fired samples are always slightly denser and less porous than the conventional counterparts. The evolution of closed porosity as a function of the bulk density is shown in **Figure 3d**. The results show the onset of close pore formation at a relative density of around 85%. The maximum amount of closed pores is achieved when the relative density is around 90%, and then also the closed porosity is removed from the system. The same pathway is followed for all the sintering conditions, i.e. conventional sintering 120 min, fast firing 120 min and fast firing 10 min.

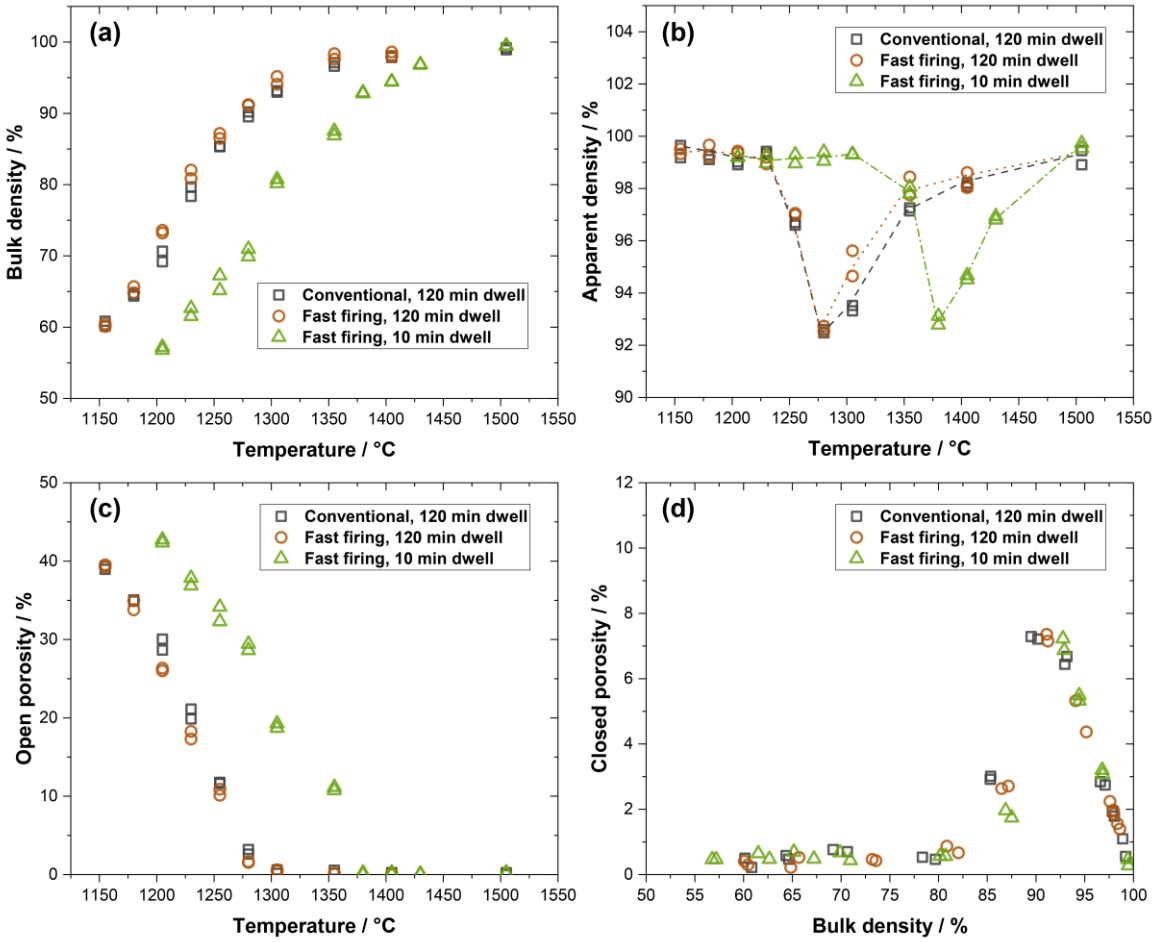

Figure 3. Relative (a) bulk and (b) apparent density and (c) open porosity as a function of the sintering temperature for the different sintering approaches. (d) closed pore evolution as a function of the relative bulk density.

3.3 Fast firing vs. master sintering curve

To correctly compare the density evolution during firing with the dilatometric results we introduced an additional thermocouple inside the furnace and performed FEM of the sample temperature evolution (**Figure 4**). The thermocouple consistently measured a temperature ≈ 5°C higher than the nominal programmed one. FEM

simulations pointed out that the equilibrium at the sample location is ≈3°C lower than that measured by the thermocouple. Hence a good match is expected between the programmed furnace temperature and the actual one. The time needed to heat up the sample as it were introduced in the hot furnace at the equilibrium is in the order of ≈7 s according to FEM (**Figure 4b**). On the other hand, when opening the furnace to introduce the pellets for FF the furnace temperature immediately dropped ≈40°C and reach again the nominal value in ≈ 1-1.5 min. Hence, we can assume that the actual sample permanence at the firing temperature for the 10 min FF experiment was ≈ 9 min.

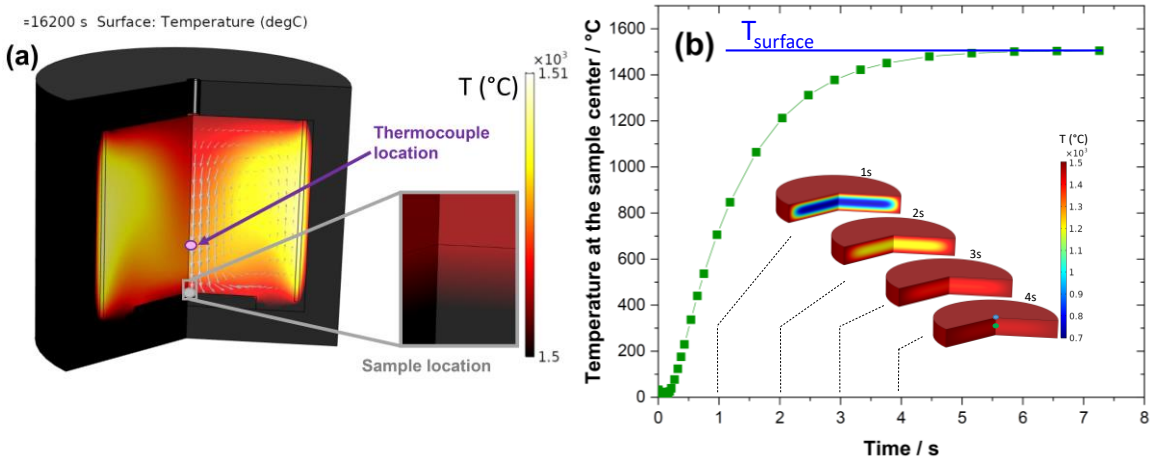

Figure 4. (a) FEM modeling of the temperature distribution inside the furnace chamber. The sample and thermocouple location are evidenced. (b) Temperature calculated by FEM at the sample center as it were quickly introduced into the furnace chamber at a constant temperature (1500°C).

$\Theta_{(T,t)}$ was calculated for the different sintering experiment using an activation energy of 650 kJ mol^{-1} (i.e., the *Q* providing the best fit of the dilatometric data, **Figure 2**). For the $\Theta_{(T,t)}$ both the heating ramp, the cooling rap and the isothermal dwell were considered in the case of conventional sintering, for fast firing only the isothermal dwell reduced by one minute was considered (i.e., to account the furnace temperature drop for introducing the specimen). The $\Theta_{(T,t)} - \rho$ relation is shown in **Figure 5** and compared with the dilatometric MSC. We can observe a quite good agreement between the sintering experiments and what extrapolated from dilatometry. However, we can also observe that the samples obtained by FF, either 10 min or 120 min, show a slightly improved densification compared to the conventionally fired materials. The difference is in any case modest, typically below 3%.

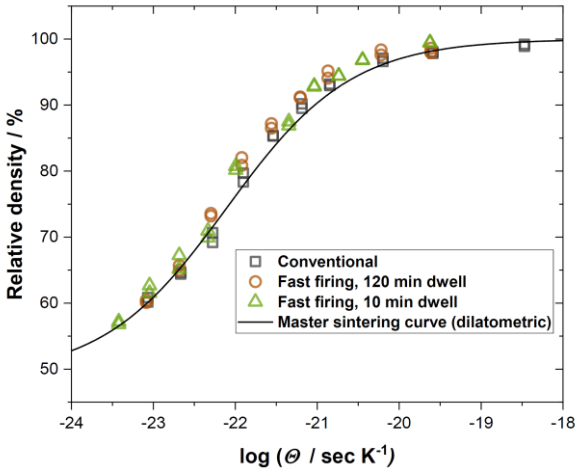

Figure 5. Comparison between the $\Theta_{(T,t)} - \rho$ plot obtained by MSC method (dilatometry) with the measured densities after sintering.

3.4 Microstructural evolution during fast firing and conventional sintering

The cumulative (open) pore size distribution as a function of the pore diameter is reported in **Figure 6a'-a'''** for samples obtained by fast firing and conventional sintering at different density levels for samples in the early and intermediate sintering stages (relative density ≈ 65- 87%). The average pore size and the standard deviation of the pore size distribution function are reported in **Figure 6b**. We can observe that the pore size tends to decrease as sintering proceeds. The differences between the different sintering approaches, i.e., conventional, FF-120min, and FF-10min, are modest. However, we can notice that the pore size for the short fast-firing approach is generally smaller than that obtained through the other sintering schedules. The main difference can be probably spotted for the samples possessing a cumulative pore volume of ≈20 $cm^3\ g^{-1}$ (relative density ≈87%) where the pore size of the conventionally sintered YSZ is substantially larger than that of FFed ceramics. This effect could indicate a slightly reduced surface diffusion in FF explaining the slight shift on the left for FF MSC plot. **Figure 6c** reports the microstructures (thermal etching) of samples in the late-intermediate and final sintering stages. No pore-grain boundary separation can be spotted and the grain size seems substantially independent of the sintering condition, without substantial grain refinement induced by rapid heating. The reported micrographs refer to the center of the sample, whose microstructure was however homogeneous throughout the cross-section.

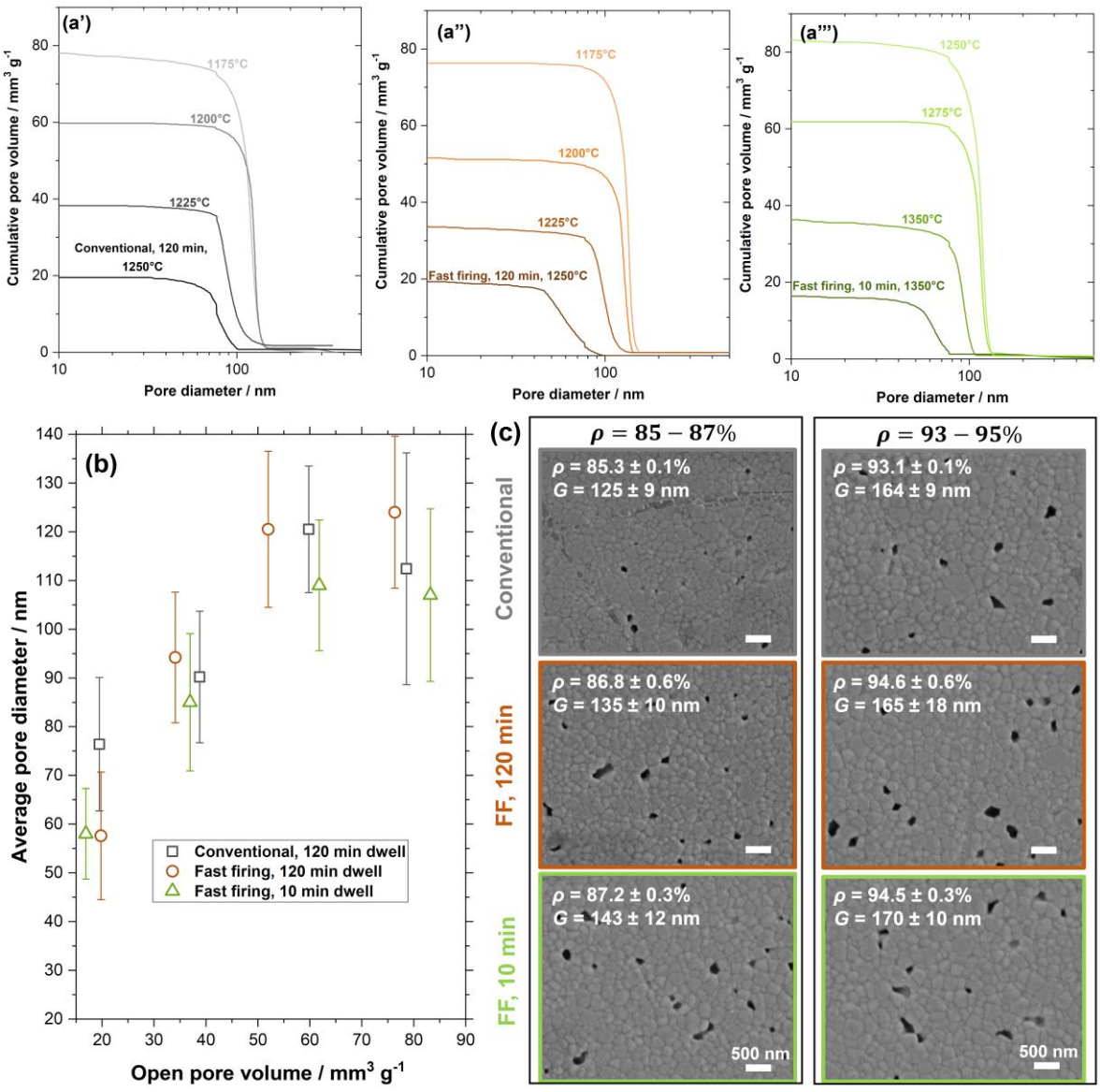

Figure 6. Cumulative pore size distribution for samples obtained by (a') conventional sintering, (a'') FF-120 min and (a''') FF-10 min. (b) average pore size as a function of the open pore volume, the error bars report the standard deviation of the pore size distribution function. (c) SEM micrographs of thermally etched samples at two different density levels.

4. Discussion

4.1 Modelling fast firing by the master sintering curves method

The MSC approach (**Figure 2b**) allows us to obtain a substantially good fitting of the dilatometric data with an apparent activation energy for densification of 650 kJ mol^{-1}. Such a value is slightly larger than previous results from the literature [30–32], usually indicating Q in the range between 500 and 600 kJ mol^{-1}. There is, however, a substantial scattering of Q data in the literature with some authors reporting larger values (even >1000 kJ mol^{-1}) [33]. Moreover, we assumed that only one densification mechanism is activated, leading to a single Q value, which is indeed an approximation as the densification mechanism (and therefore Q) might change during sintering [32]. The activation energy measured in this work, however, well matches the results reported in reference [24] where the MSC was calculated for a coarser 3YSZ powder from the same manufacturer.

The key outcome of this work is that when considering 40 nm-sized 3YSZ powder the heating rate plays a role in sintering; however, the effect is modest (no more than ≈2-3% in terms of relative density). Such a conclusion is supported by the good match of the densification pathway (**Figure 3a,b,c**) between samples obtained by conventional sintering and fast-fired for 120 min. More importantly, if we consider the results in the $\Theta_{(T,t)} - \rho$ plot (**Figure 5**), conventional sintering, FF-120 min, and FF-10 min results converge, though a small improvement can still be detected in the case of rapid sintering. The fact that the samples FFed for only 10 min do not substantially overperform the one FFed for 120 min suggests that the formation of

transient non-equilibrium grain boundaries or impurities-related liquid phase do not play a major role in this specific system (mechanisms iii and iv in the Introduction).

A similar behavior can be spotted also in the case of different choices of *Q*. In particular, **Figure S1** reports the dilatometric MSC for the typical activation energies reported in the literature for YSZ (500 and 600 kJ mol^{-1}). We can observe that the FFed samples slightly overperform the conventional ones regardless of the choice of *Q* (within a reasonable range). When considering a relatively low activation energy (500 kJ mol^{-1}) the short fast firing cycle seems more effective, however, the results are likely biased by an inappropriate choice of the activation energy as conventionally sintered materials do not fit properly the dilatometric MSC (**Figure S1b**).

Note that herein we used the same activation energy for rapid and slow heating. This assumption is based on the fact that *Q* represents the activation energy for the diffusion of the slowest species (in this case cations) through the fasted path (lattice or grain boundary). Therefore, it is not expected to be influenced by the pore size and geometry that could change as a result of surface diffusion under low heating rates. A change of *Q* would signal a change in the densification mechanisms, like a transition between grain boundary and lattice diffusion (or the formation of out-of-equilibrium grain boundary or transient liquid phases) which might take place if there is a substantial difference in the microstructural scale under different sintering approaches. For instance, the strain rate in the combined sintering stage model by Hansen et al. [34] scales with G^{-n}, *n* being 3 for lattice diffusion and 4 for grain boundary

diffusion. Indeed, if FF and conventional sintering lead to substantially different *G* at the same density level, then we could expect a change in the densification mechanism and in *Q*. However, the results in **Figure 6** do not match the assumption that the heating rate causes a substantial change in the microstructural scale of the material tested in this work. This is confirmed by the relatively good match between the dilatometric MSC and the FFed samples, a change in the densification mechanism would in fact cause a substantial deviation between them.

Besides densification, the dynamic of closed pore formation and the related transition from the intermediate to the final sintering stages is weakly affected by the sintering rate as evidenced in **Figure 3d**.

The substantial match between the MSC and the results obtained by FF suggests that the hypothesis underlying the MSC model still holds on in this work. Among them, the idea that "*the microstructure depends on the density only and is independent of the thermal history*" is the key one. Such a conclusion is supported by the data in **Figure 5** where we observe that the pore size vs. pore volume plot is rather similar for rapid and conventional sintering. The differences in terms of pore size at a similar density level are in most of the cases <10% and still within the scattering of experimental data. Besides this, it seems that the samples obtained by FF-10 min possess a systematically smaller pore size, thus probably explaining the modest improvement in the sintering behavior observed under rapid sintering. Also, the microstructures obtained in the final and late-intermediate sintering stages support the conclusion that the heating rate has a modest impact on the grain size

and microstructure. In other words, the observed microstructural evolution agrees well with the MSC and density results.

Looking behind the literature, we can observe that these results on 40 nm-sized 3YSZ lay in between two previous works on UHS on 90 nm and 20 nm-sized powder [18, 24]. The work on the coarser powder has shown a good agreement with the densification pathway obtained by UHS and the MSC [24]. On the other hand, when considering small nanopowders (20 nm) a “spectacular” acceleration of sintering has been detected and this has been attributed to a substantial reduction in the grain and pore size (rapid sintering leading to grain size just above 1/3 of the conventionally sintered materials for a given density level). Rapid heating-promoted sintering was also reported by Kocjan on ≈100 nm YSZ particles, though also their case the crystallite size was very small (27 nm) [35]. In summary, rapid heating can enhance the densification of YSZ but the effect is clearly detectable only for very small particle sizes, ideally in the order of 20-30 nm. The heating rate effects are already quite faint when 40 nm particles are considered.

4.2 On the fast firing effect on the stress intensification function

The small improvement (left shift) in the fast-firing MSC plot also highlights the fact that the MSC method is insensitive to the magnitude of the stress intensification function for 40 nm 3YSZ powder. Indeed, the activation energy is identified on the simple hypothesis that the density function $\int_{\rho_0}^{\rho} \frac{G(\rho)^m}{\rho\Gamma(\rho)} d\rho$ is unique whatever the thermal schedule is. Consequently, the MSC cannot be disturbed by erroneous $\Gamma(\rho)$

theoretical functions. The latter, often assume dominant surface diffusion with spherical porosity and are known to be far from the experimental behavior [23, 36]. The stress intensification factor can be estimated from bulk modulus ($\psi(\rho)$) using the expression $\Gamma(\rho) = \frac{\rho^2}{\psi(\rho)}$. Different theoretical moduli can be taken to calculate $\Gamma(\rho)$ like Skorohod [37], Sofronis & McMeeking [38], Green [39], *etc*. In **Figure 7a**, the $\Gamma(\rho)$ term of Skorohod is compared to an experimental one determined by conventional sintering on the same powder of this study [40] (with $\psi = \frac{2}{3}\frac{(-0.4165+\rho)^3}{1-\rho}$). It is clear from this graph that the experimental term $\Gamma(\rho)$ is significantly higher than the theory predicted from spherical porosity. It is possible to report this difference in a MSC graph by moving the constant terms on the right hand side of **Eq. 4** and assuming a modest grain growth ($G \sim G_0$) in the intermediate stage.

$$\int_{\rho_0}^{\rho} \frac{1}{\rho\Gamma(\rho)}\, d\rho = \frac{3\gamma\Omega D_0}{k{G_0}^m} \int_0^t \frac{1}{T} exp\left(\frac{-Q}{RT}\right) dt \qquad (5)$$

A similar of MSC graph can then be plotted by calculating the term $ln\left(\int_{\rho_0}^{\rho} \frac{1}{\rho\Gamma(\rho)}\, d\rho\right)$ for each $\Gamma(\rho)$ experimental/theoretical functions. The result is reported in **Figure 7b**. This shows the experimental term $\Gamma(\rho)$ is significantly more responsive than the theoretical which is significantly shifted to the right (black arrow).

This example helps decompose to most effective mechanisms responsible for fast sintering of real microstructures. The great difference is between the theoretical and experimental term $\Gamma(\rho)$ which implies a significant shift of the MSC curve to the left,

even for conventional sintering. This points out real microstructures are highly responsive and greatly underestimated by the theory. Consequently, the fast firing that improves only 2-3% of relative density implicates a very limited improvement and a small additional shift to the left in the MSC plot. This modest improvement is then the logical consequence of the high responsiveness of the real porous geometries that does not have a high amplitude of responsiveness improvement. Based on this, we can conclude that a careful experimental identification of the term $\Gamma(\rho)$ should be enough to model (ultra)rapid sintering kinetics for the powder studied in this work. A similar result has been obtained for Flash SPS [22] where the experimentally determined sintering moduli were enough to simulate the ultra-rapid densification curves without additional improvement of the sintering kinetics.

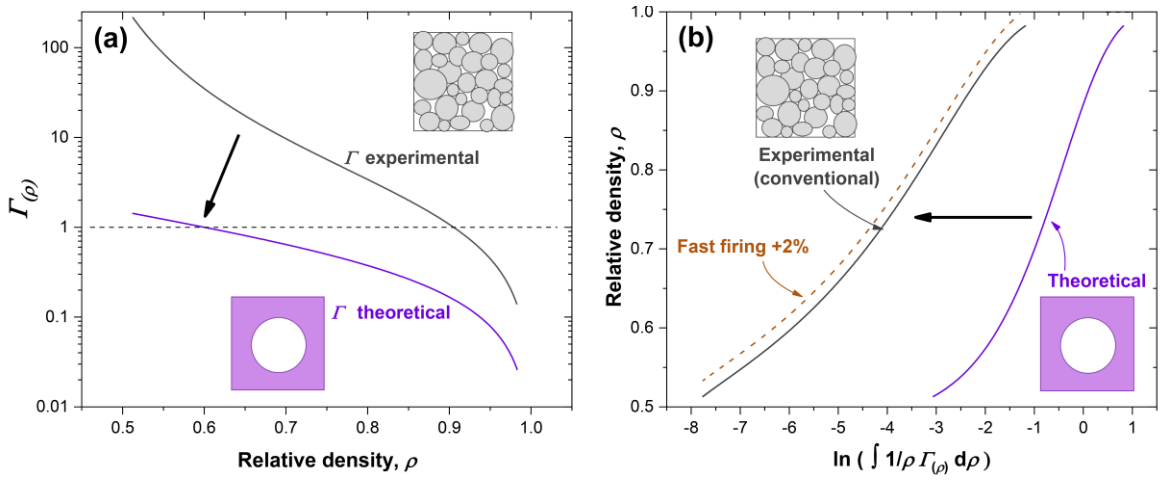

Figure 7. Illustration of the differences of stress intensification factor between the theoretical approach assuming dominant surface diffusion and experimental values. (a) represents the $\Gamma(\rho)$ terms; (b) the equivalent corresponding MSC plot, the gray dotted curve is a curve with the 2% increase of relative density which correspond the

experimental shift in density with conventional MSC. It shows the small improvement of fast firing compared to the significant error if simplified pore geometry is used.

5. Conclusions

Rapid heating plays a small role in promoting the densification of 40 nm-sized 3YSZ powder in open air. In general, fast firing allows to improve the final density by no more than 2-3%. As such, the densification pathway can be modeled using the master sintering curve extrapolated from dilatometric data. No major differences can be spotted also considering the dynamic of closed pores formation at the onset of the final sintering stage. This moderate effect is due to the fact that real porous geometries are highly responsive even for conventional sintering. Consequently, the highly responsive pore geometry has modest surface diffusion reducing the improvement amplitude for additional surface diffusion reduction by fast firing. This conclusion is based on the sintering behavior of 40 nm-sized YSZ powder and might not hold on for material with highly active surface diffusion or different particle size.

The densification behavior upon FF and its relatively good match with the master sintering curve prediction is consistent with the observed modest impact of the heating rate on the final microstructure. Comparing our data with literature results, it is argued that the rapid firing-promoted densification is a phenomenon pivotal only when extremelly fine 3YSZ nanopowders are considered (<30 nm).

Acknowledgments

Mr. Enrico Kambo, Jonathan Selorm Degbedzui, and Livio Zottele are warmly acknowledged for their experimental work and support.

References

1. Rahaman MN. Ceramics Processing and Sintering. 2end ed. 2end ed. Marcel Dekker, New York; 1995 https://doi.org/https://doi.org/10.1201/9781315274126
2. Biesuz M, Grasso S, Sglavo VM. What's new in ceramics sintering? A short report on the latest trends and future prospects. *Curr Opin Solid State Mater Sci*. 2020;24(5):100868. https://doi.org/10.1016/j.cossms.2020.100868
3. Biesuz M, Sglavo VM. Flash sintering of ceramics. *J Eur Ceram Soc*. 2019;39(2–3):115–143. https://doi.org/10.1016/j.jeurceramsoc.2018.08.048
4. Yu M, Grasso S, Mckinnon R, Saunders T, Reece MJ. Review of flash sintering: materials, mechanisms and modelling. *Advances in Applied Ceramics*. 2017;116(1):24–60. https://doi.org/10.1080/17436753.2016.1251051
5. Dancer CEJ. Flash sintering of ceramic materials. *Mater Res Express*. 2016;3:102001.
6. Cologna M, Rashkova B, Raj R. Flash sintering of nanograin zirconia in <5 s at 850°C. *Journal of the American Ceramic Society*. 2010;93(11):3556–3559.
7. Guillon O, Gonzalez-Julian J, Dargatz B, *et al.* Field-assisted sintering technology/spark plasma sintering: Mechanisms, materials, and technology developments. *Adv Eng Mater*. 2014;16(7):830–849. https://doi.org/10.1002/adem.201300409
8. Chaim R, Chevallier G, Weibel A, Estournès C. Grain growth during spark plasma and flash sintering of ceramic nanoparticles : a review. *J Mater Sci*. 2018;53:3087–3105. https://doi.org/10.1007/s10853-017-1761-7
9. Orrù R, Licheri R, Locci AM, Cincotti A, Cao G. Consolidation/synthesis of materials by electric current activated/assisted sintering. *Materials Science and Engineering R*. 2009;63:127–287. https://doi.org/10.1016/j.mser.2008.09.003
10. Grasso S, Sakka Y, Maizza G. Electric current activated/assisted sintering (ECAS): a review of patents 1906–2008. *Sci Technol Adv Mater*. 2009;10(5):53001.
11. Oghbaei M, Mirzaee O. Microwave versus conventional sintering: A review of fundamentals, advantages and applications. *J Alloys Compd*. 2010;494(1–2):175–189. https://doi.org/10.1016/j.jallcom.2010.01.068
12. Katz JD. Microwave Sintering of Ceramics. *Annual Review of Materials Science*. 1992;22:153–170.
13. Wang C, Ping W, Bai Q, *et al.* A general method to synthesize and sinter bulk ceramics in seconds. *Science (1979)*. 2020;368(6490):521–526. https://doi.org/10.1126/science.aaz7681
14. Kermani M, Hu C, Grasso S. From pit fire to Ultrafast High-temperature Sintering (UHS): A review on ultrarapid consolidation. *Ceram Int*. 2023;49(3):4017–4029. https://doi.org/10.1016/j.ceramint.2022.11.091
15. Zhang Y, Nie J, Chan JM, Luo J. Probing the densification mechanisms during flash sintering of ZnO. *Acta Mater*. 2017;125:465–475.

16. Ji W, Zhang J, Wang W, Fu Z, Todd RI. The microstructural origin of rapid densification in 3YSZ during ultra-fast firing with or without an electric field. *J Eur Ceram Soc*. 2020;40(15):5829–5836. https://doi.org/10.1016/j.jeurceramsoc.2020.07.027
17. Ji W, Parker B, Falco S, Zhang JY, Fu ZY, Todd RI. Ultra-fast firing: Effect of heating rate on sintering of 3YSZ, with and without an electric field. *J Eur Ceram Soc*. 2017;37:2547–2551.
18. Biesuz M, Hérisson de Beauvoir T, De Bona E, *et al.* Ultrafast high-temperature sintering (UHS) vs. conventional sintering of 3YSZ: Microstructure and properties. *J Eur Ceram Soc*. 2024;44(7):4741–4750. https://doi.org/10.1016/j.jeurceramsoc.2024.01.064
19. Wang S, Mishra TP, Deng Y, *et al.* Electric Current-Assisted Sintering of 8YSZ: A Comparative Study of Ultrafast High-Temperature Sintering and Flash Sintering. *Adv Eng Mater*. 2023;2300145. https://doi.org/10.1002/adem.202300145
20. Zhang J, Meng F, Todd RI, Fu Z. The nature of grain boundaries in alumina fabricated by fast sintering. *Scr Mater*. 2010;62:658–661.
21. Olevsky EA, Kandukuri S, Froyen L. Consolidation enhancement in spark-plasma sintering: Impact of high heating rates. *J Appl Phys*. 2007;102(11). https://doi.org/10.1063/1.2822189
22. Manière C, Harnois C, Marinel S. Role of microstructure reactivity and surface diffusion in explaining flash (ultra-rapid) sintering kinetics. *J Eur Ceram Soc*. 2023;43(5):2057–2068. https://doi.org/10.1016/j.jeurceramsoc.2022.12.006
23. Su H, Johnson DL. Master Sintering Curve: A Practical Approach to Sintering. *Journal of the American Ceramic Society*. 1996;79(12):3211–3217. https://doi.org/10.1111/j.1151-2916.1996.tb08097.x
24. Dong J, Pouchly V, Biesuz M, *et al.* Thermally-insulated ultra-fast high temperature sintering (UHS) of zirconia: A master sintering curve analysis. *Scr Mater*. 2021;203:114076. https://doi.org/10.1016/j.scriptamat.2021.114076
25. Guillon O, Langer J. Master sintering curve applied to the Field-Assisted Sintering Technique. *J Mater Sci*. 2010;45(19):5191–5195. https://doi.org/10.1007/s10853-010-4556-7
26. Balice L, Cologna M, Audubert F, Hazemann J-L. Densification mechanisms of UO2 consolidated by spark plasma sintering. *J Eur Ceram Soc*. 2021;41(1):719–728. https://doi.org/10.1016/j.jeurceramsoc.2020.07.002
27. Manière C, Zahrah T, Olevsky EA. Fluid dynamics thermo-mechanical simulation of sintering: Uniformity of temperature and density distributions. *Appl Therm Eng*. 2017;123:603–613. https://doi.org/10.1016/j.applthermaleng.2017.05.116
28. https://ep.liu.se/en/conference-article.aspx?series=ecp&issue=27&Article_No=23. n.d.
29. Rybakov KI, Olevsky EA, Krikun E V. Microwave sintering: Fundamentals and modeling. *Journal of the American Ceramic Society*. 2013;96(4):1003–1020. https://doi.org/10.1111/jace.12278
30. Caruso R, Mamana N, Benavidez E. Densification kinetics of ZrO2-based ceramics using a master sintering curve. *J Alloys Compd*. 2010;495(2):570–573. https://doi.org/10.1016/j.jallcom.2009.11.080
31. Mazaheri M, Simchi A, Dourandish M, Golestani-Fard F. Master sintering curves of a nanoscale 3Y-TZP powder compacts. *Ceram Int*. 2009;35(2):547–554. https://doi.org/10.1016/j.ceramint.2008.01.008
32. Kocjan A, Pouchly V, Shen Z. Processing of zirconia nanoceramics from a coarse powder. *J Eur Ceram Soc*. 2015;35(4):1285–1295. https://doi.org/10.1016/j.jeurceramsoc.2014.10.022

33. Pouchly V, Maca K, Shen Z. Two-stage master sintering curve applied to two-step sintering of oxide ceramics. *J Eur Ceram Soc*. 2013;33(12):2275–2283. https://doi.org/10.1016/j.jeurceramsoc.2013.01.020
34. Hansen JD, Rusin RP, Teng M-H, Johnson DL. Combined-Stage Sintering Model. *Journal of the American Ceramic Society*. 1992;75(5):1129–1135. https://doi.org/10.1111/j.1151-2916.1992.tb05549.x
35. Kocjan A, Logar M, Shen Z. The agglomeration, coalescence and sliding of nanoparticles, leading to the rapid sintering of zirconia nanoceramics. *Sci Rep*. 2017;7(1):2541. https://doi.org/10.1038/s41598-017-02760-7
36. Manière C, Harnois C, Marinel S. Porous stage assessment of pressure assisted sintering modeling parameters: a ceramic identification method insensitive to final stage grain growth disturbance. *Acta Mater*. 2021;211:116899. https://doi.org/10.1016/j.actamat.2021.116899
37. Olevsky EA. Theory of sintering: from discrete to continuum. *Materials Science and Engineering: R: Reports*. 1998;23(2):41–100. https://doi.org/10.1016/S0927-796X(98)00009-6
38. Sofronis P, McMeeking RM. Creep of Power-Law Material Containing Spherical Voids. *J Appl Mech*. 1992;59(2S):S88–S95. https://doi.org/10.1115/1.2899512
39. Green RJ. A plasticity theory for porous solids. *Int J Mech Sci*. 1972;14(4):215–224. https://doi.org/10.1016/0020-7403(72)90063-X
40. Manière C, Grippi T, Marinel S. Estimate microstructure development from sintering shrinkage: A kinetic field approach. *Mater Today Commun*. 2022;31:103269. https://doi.org/10.1016/j.mtcomm.2022.103269